COMPUTER METHODS IN MATERIALS SCIENCE

2023, vol. 23, no. 4, 45–56
https://doi.org/10.7494/cmms.2023.4.0822

Numerical modelling of continuous laser welding of S355J2 steel using a volumetric heat source

Aleksander Siwek[1]*, Sławomir Kąc[1], Janusz Pikuła[2]

[1] AGH University of Krakow, al. A. Mickiewicza 30, 30-059 Krakow, Poland.
[2] Łukasiewicz Research Network – Upper Silesian Institute of Technology, ul. Karola Miarki 12–14, 44-100 Gliwice, Poland.

Abstract

Numerical modelling of laser welding requires that numerous strongly coupled physical phenomena be taken into account. A laser is a source of welding heat characterized by the small size of the heating volume and the shape of the fusion zone has a marked impact on the quality of the weld. In this work, a conical heat source was used with geometrical parameters to give the appropriate profile of the fusion line. The use of the weld shape factor and the dependence of the power density on the linear welding energy increases the accuracy of matching the calculated shape of the fusion line. The heat source was tested for the continuous welding case of a sheet made of steel type S355J2. The CFD software ANSYS Fluent was used to calculate the welding model. The temperature field, calculated using the finite volume method, was used to calculate the phase composition and fusion zone profile tracking. The nodes of the model reaching the maximum solidus temperature of S355J2 steel, form the profile of the fusion zone. The laser welding model allows for tracking of the kinetics of phase transformations in the cooling stage. Continuous cooling transformation phase diagram data is loaded for the welded steel grade. The calculation results of the welding model were compared with the weld micrographs.

Keywords: laser welding, numerical modelling, CFD, conical heat source, phase changes in steel

1. Introduction

During laser welding, energy concentrated in a small volume of material causes rapid thermal processes to occur. Numerical modelling is an important tool for analyzing processes of this type (Dal & Fabbro, 2016; Farrokhi et al., 2019). Welding efficiency depends significantly on the process parameters selected for the particular case (Yan et al., 2022). The impact of the energy supplied by the laser is limited to areas directly illuminated by the beam. The influence of welding on the structure and properties of the weld depends on the thermophysical properties of the steel. To achieve good quality welds, numerous experimental trials to find the optimal combination of process parameters are required (Pyo et al., 2022). Considering the above, numerical modeling must concern both the temperature field and the fluid flow in the weld pool. The temperature field obtained from such a model can be used to calculate phase transitions occurring during thermal cycles in the heat-affected zone (HAZ).

An important element of the welding model is the heat source and the energy supplied to the parts being welded melts the volume of material directly affected by the laser. Convection of liquid metal takes place in the created weld pool, the Marangoni effect forces

*Corresponding author: Aleksander.Siwek@agh.edu.pl
ORCID ID's: 0000-0003-3507-2859 (A. Siwek), 0000-0001-9556-2345 (S. Kąc), 0000-0003-3312-7537 (J. Pikuła)

the weld pool surface flow, the metal evaporates, and finally, phase changes occur depending on the different cooling rates (Ha & Kim, 2005; Jie & Hui, 2018). The first simplified models assumes a point heat source and constant material properties (Rosenthal, 1941). Another group assumes a surface source with a Gaussian profile or depending on the applied laser mode (Han & Liou, 2004; Tsai & Eagar, 1985). The development of numerical methods based on the finite element method (FEM) and finite volume method (FVM) initiated the development of volumetric heat sources in modelling of welding (Bag et al., 2009; Goldak et al., 1984; Wu et al., 2009). Volumetric heat source models contain geometrical parameters whose values should be selected accordingly. The basic source of data needed to match the fusion zone (FZ) to experimental results are the measurements of the fusion line obtained on metallographic specimens (Mollamahmutoglu & Yilmaz, 2021). The FZ and the HAZ are visible on the etched metallographic specimen. Microhardness measurements in the welding area permit the determination of the phases formed during the welding process (Ai et al., 2016; Chen et al., 2019; Esfahani et al., 2014). The choice of heat source model adopted has a crucial influence on the shape of the calculated weld and thus it is justified to optimize the parameters of the volume heat source which have been verified by microstructure measurements.

The accuracy of the welding model depends on how advanced the model is, i.e. taking into account physical phenomena, numerical method of solving differential equations and mesh density used in the model (Liu et al., 2023). There are two approaches to the issue of physical phenomena occurring during welding. A simplified form is to consider only the heat conduction equation but such an approach is inaccurate and only approximately predicts the FZ shape (Kumar & DebRoy, 2004; Safdar et al., 2007). The second approach additionally takes into account the momentum and mass conservation equation. This makes it possible to take into account the Marangoni phenomenon and convection heat flow in the weld pool (Mukherjee et al., 2017; Siwek, 2021). Simplifying the model by omitting the momentum and surface tension conservation equations reduces the accuracy of the calculated fusion line. Convection forced by surface tension changes the shape of the fusion line and the size of the weld.

The paper presents the use of a conical heat source model in a laser welding simulation. The correctness of the model was checked for the S355J2 steel welded at several speeds and laser powers. Since position measurements of numerous points along the fusion line on micrographs is both cumbersome and time-consuming, weld shape measurements were limited to the radius and depth of the fusion zone. The model calculations were performed with the ANSYS Fluent software. The use of process symmetry plane, non-uniform mesh and parallelization of calculations reduced the computation time. The model includes phase transformations in steel and the associated volumetric heat source.

The aim of the work is to build a welding model with a volumetric heat source and then optimize the source parameters to obtain the smallest possible error. It was assumed that limiting the parameters to the height and radius of the weld is sufficient to obtain good agreement with the microstructure measurements. Reducing the number of optimization parameters speeds up the process of obtaining the correct result. An additional goal was to examine the correctness of the surface tension boundary condition due to the calculated shape of the fusion line.

2. Model of welding

A numerical model was developed to investigate the volumetric heat source. The model of the plate with dimensions of 50 mm × 50 mm × 12 mm is shown schematically in Figure 1. Calculations were performed only for half of the geometry by using symmetry conditions. This assumption reduces the number of model finite volumes. The hexahedral unstructured mesh used in the model is shown in Figure 2. For all welding parameters, the mesh density was increased in the vicinity of the weld pool to achieve convergence and increase the accuracy of the numerical solution. The welding plane, which is also the symmetry plane, is determined by the y–z axes (Fig. 2). The welding energy is delivered to the model by a laser beam and, in this work, a conical shape for the heat source was used. The greatest possible similarity of the shape and size of the FZ, with images of the FZ calculated and measured on metallographic sections, was achieved by minimizing the square errors of the measurement data.

The laser beam's energy is partly absorbed at the irradiation surface and partly reflected by the surface. The absorption coefficient (η) varies significantly depending on the surface condition, temperature and the presence of plasma above the weld pool (Laurens et al., 1996; Semak et al., 2000). In the work, a constant value of the absorption coefficient was assumed, the value of which is presented in Table 1.

For high laser power densities, the free surface of the weld pool deviates from the plane (Ki et al., 2002). The model does not consider the laser beam's interaction with the surface, such as the recoil pressure of evaporating steel from the surface (Semak & Matsunawa, 1997).

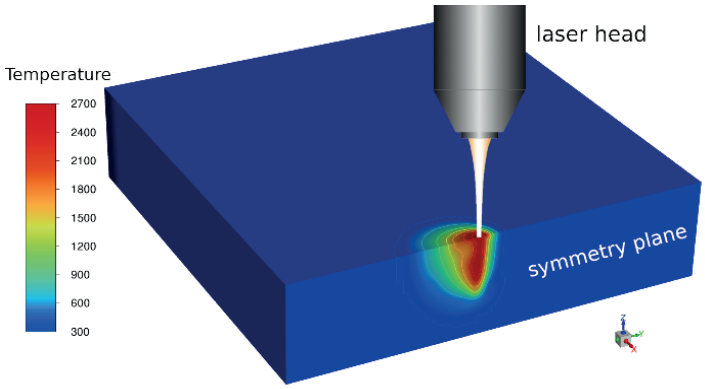

Fig. 1. Schematic diagram of laser welding of a plate with dimensions of 50 mm × 50 mm × 12 mm

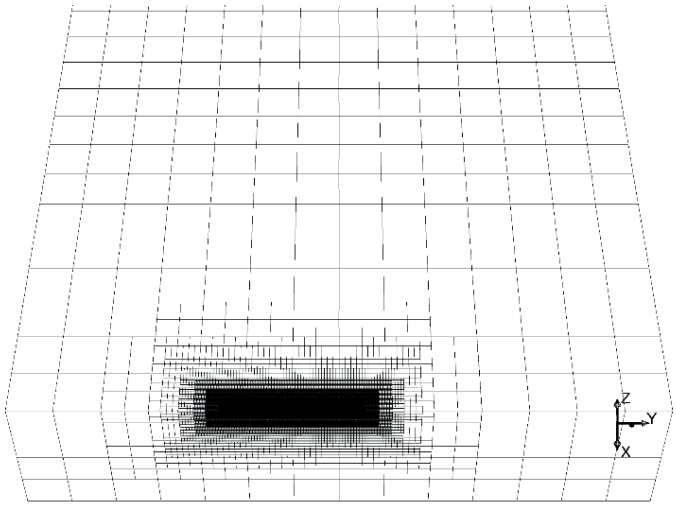

Fig. 2. Finite volume hexahedral mesh with refinement in the weld area

Table 1. Thermo-physical properties of S355J2 steel (BS-EN1993-1-2, 2005; Han & Liou, 2004; Sahoo et al., 1988)

Symbol	Description	Value
T_s	solidus temperature	1750 K
T_l	liquidus temperature	1800 K
ρ	density	7850 kg/m^3
k	thermal conductivity	55 W/(m·K)
c_p	specific heat	500 J/(kg·K)
μ_l	dynamic viscosity of fluid	0.0055 kg/(m·s)
a	laser beam radius	0.0004 m
η	absorption coefficient	0.5
ε	radiation coefficient	0.6
h	heat transfer coefficient	20 W/(m·K)
A	temperature coefficient of surface tension	$-0.43 \cdot 10^{-3}$ N/(m·K)
Γ_s	surface excess at saturation	$0.13 \cdot 10^{-6}$ mol/m^2
k_1	entropy factor	$3.18 \cdot 10^{-3}$
$\Delta H°$	enthalpy of adsorption	$-166.2 \cdot 10^3$ J/mol

3. Experimental procedures and modelling

Welding tests were carried out on a robotic stand equipped with a Trumpf disk laser – TruDisk 12002 with a Trumpf D70 head for laser welding, mounted on a KUKA KR30HA industrial robot (Fig. 3). The applied welding device enables continuous welding with various parameters. The model was tested on S355J2 steel, the composition of which was analyzed using the optical emission spectrometry method with spark excitation on a Q4 TASMAN stationary spectrometer by Bruker. The measurement results are presented in Table 2. The steel sample was in the form of a 12 mm thick plate. Continuous welding tests were carried out with a 1–5 kW laser beam at speeds of 0.5 and 1.0 m/min. The bead length for each weld test was 35 mm.

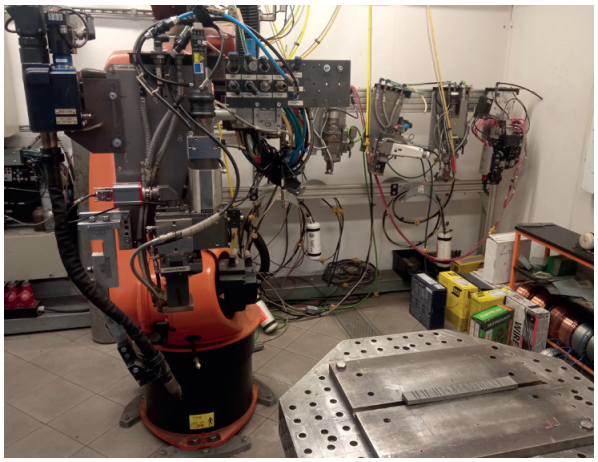

Fig. 3. Robotic welding station equipped with a disc laser TruDisk 12002

Table 2. Chemical composition [wt.%] of S355J2 steel

C	Si	Mn	P	S	Cu
0.133	0.012	1.293	0.010	0.008	0.025

As previously mentioned, a conical heat source was used for the numerical modelling. It is a three-dimensional heat source with an intensity distribution varying along the depth of the sample. The power distribution of the source changes, from the maximum on the welded surface to the minimum on the other base of the conical heat source, depending on the depth parameter of this source (Fig. 4). The radius of the heat source decreases linearly with the depth from the welded surface. The work uses the conical power density profile $\dot{Q}$ proposed by Wu et al. (2006) described by the following equation:

$$\dot{Q}(r,z) = \frac{9\eta P}{\pi(1-e^{-3})}\frac{1}{(z_e-z_i)(r_e^2+r_e r_i+r_i^2)}\exp\left[-3\left(\frac{r}{r_0}\right)^2\right] \quad (1)$$

where η is the absorption coefficient, P is the laser beam power, r is the distance to the laser beam axis, z is the distance from the upper welding surface and z_e, z_i are the coordinates of the upper, and lower base of the conical heat source.

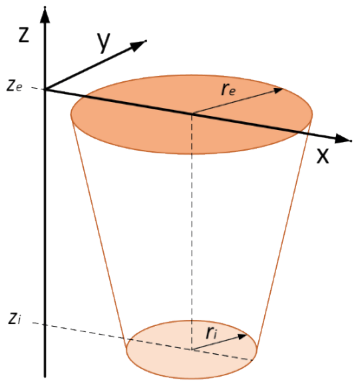

Fig. 4. Scheme of the volume heat source

As can be seen from Equation (1), the maximum value of the power density in the axis of the laser beam $\dot{Q}(0,z)$ remains constant over the entire conical source depth. The radius of the conical heat source r_0 decreases linearly, depending on the z coordinate according to the equation:

$$r_0(z) = r_e - (r_e - r_i)\frac{z_e - z}{z_e - z_i} \quad (2)$$

A weld pool is created in the laser impact area. The boundary condition of the energy conservation equations at the weld surface of the sample includes energy loss by convection, radiation, and latent heat of vaporization. This condition is described by the equation:

$$-k\frac{\partial T}{\partial \vec{n}} = -h(T-T_a) - \sigma\varepsilon(T^4 - T_a^4) - q_{ev} \quad (3)$$

where k is the coefficient of conductivity, $\vec{n}$ is the versor normal to the weld pool surface, h is the coefficient of convection, σ is the Stefan–Boltzmann constant, ε is the radiation emissivity, T_a is the ambient temperature in Kelvin, and q_{ev} is the vaporization heat.

On the remaining surfaces of the sample, energy is dissipated into the environment by convection and radiation:

$$-k\frac{\partial T}{\partial \vec{n}} = -h(T-T_a) - \sigma\varepsilon(T^4 - T_a^4) \quad (4)$$

The laser used in the model as a welding heat source, creates a large temperature gradient. This in turn induces a surface tension gradient across the free surface of the weld pool. Liquid circulation in the entire volume of the weld pool is forced, among others, by surface tension distribution. The shear stress on the liquid surface can be expressed as:

$$\tau_{\vec{s}} = \mu_l \frac{\partial(\vec{V}\cdot\vec{s})}{\partial\vec{n}} = f_l \frac{\partial\gamma}{\partial T}\frac{\partial T}{\partial\vec{s}} \tag{5}$$

where $\vec{V}$ is the velocity, $\vec{s}$ is the versor tangent to the liquid surface, μ_l is the dynamic viscosity of the liquid, γ is the surface tension, and f_l is the liquid volume fraction.

Surface tension described by Equation (6) depends on the temperature field and the sulfur concentration on the surface of the weld pool. The model assumes that the weld pool surface stays flat throughout the welding process for the laser power range used in the model. The temperature field in the sample is calculated using the energy conservation equation (Zhang et al., 2004). For the calculated temperature field, the surface temperature gradient $\partial T/\partial\vec{s}$ and the temperature coefficient of surface tension $\partial\gamma/\partial T$ are calculated in each time step of the simulations. The surface tension coefficient is described by the equations (Sahoo et al., 1988):

$$\frac{\partial\gamma}{\partial T} = -A - R\Gamma_s \ln[1+K c_i] - \frac{K c_i}{(1+K c_i)}\frac{\Gamma_s \Delta H^{\circ}}{T} \tag{6}$$

$$K = k_1 e^{-(\Delta H^{\circ}/RT)}$$

where A is temperature coefficient of pure metal, T is the melting temperature, Γ_s is the surface excess at saturation, k_1 is the constant related to the entropy of segregation, c_i is the activity of sulfur, $\Delta H°$ is the standard heat of adsorption, R is the gas constant, and K is the equilibrium constant for segregation. In this model, sulfur was the only surface-active element. Weight fraction of sulfur in S355J2 steel is presented in Table 2. The values used to calculate Equation (6) are listed in Table 1.

As can be seen from Equations (5) and (6), the direction and value of the force inducing the flow in the weld pool depends mainly on the temperature gradient and the content of the surface active element. The forced flow of energy in the weld pool determines the volume of the FZ and its shape.

For the previously described boundary and initial conditions, the solution of the welding model is based on the calculation of the temperature and velocity field of the liquid in the weld pool. The model calculations were performed with the ANSYS Fluent program package (ANSYS, 2021). Conservation equations of energy, moment and mass are solved by ANSYS Fluent using FVM. For the welding parameters used in the model, the predicted Reynolds number exceeded 500. Therefore, the standard k – ε turbulent model was chosen to calculate the flow. The energy conservation equation has the following form (ANSYS, 2021):

$$\frac{\partial(\rho E)}{\partial t} + \nabla\cdot(\vec{v}(\rho E + p)) = \nabla\cdot(k_{eff}\nabla T + \overline{\overline{\tau}}\cdot\vec{v}) + S_h \tag{7}$$

where E is the energy ($E = h - p/(\rho + 0.5v^2)$), h is the enthalpy, p is the pressure, $k_{eff} = k + k_t$ is the effective conductivity, k_t is the turbulent thermal conductivity, $\overline{\overline{\tau}}$ is the viscosity tensor, and S_h is the heat source. The volumetric heat source from the laser (Equation (1) and (2)) and the boundary conditions of the model (Equations (3)–(6)) were added to the energy equation using user-defined function (UDF).

In the welding process, the austenite formed in the heating stage undergoes phase changes in the cooling stage. The volume of material in which phase changes occur is the heat source described by the following equation:

$$\dot{q}_{v,i} = \Delta H_i \frac{\Delta X_i}{\Delta t} \tag{8}$$

where ΔH_i is the phase (i) enthalpy of transformation, ΔX_i is the phase (i) increase in time Δt.

The welding area was divided by a hexagonal mesh into finite volume cells. Obtaining an accurate and convergent solution required the use of a non-uniform mesh. In continuous welding, the size of the mesh elements increases with the distance from the symmetry plane. The stability of the solution was tested depending on the time step and the minimum size of elements in FZ. As a result of the tests, an optimal size distribution of elements was obtained. The size of the elements ranged from 0.02 mm to 2.6 mm (Fig. 2). A fixed time step of 10^{-3} s was used.

During welding, finite volumes undergo different thermal cycles depending on the distance from the welding line and the welding parameters. During heating, after exceeding the A_{c1} temperature, the structure of the steel changes into austenitic. After reaching the A_{c3} temperature, the volume fraction of austenite is 100%. When the maximum temperature is reached, mesh cells cool down at different rates (Siwek, 2021). During the cooling stage of the S355J2 steel from the austenitization temperature, ferritic and bainitic transformations as well as diffusionless martensitic transformation may occur. The volume fraction of these phases is calculated in each time step using the Johnson–Mehl–Avrami–Kolmogorov (JMAK) equations (Avrami, 1939)

and the Koistinen–Marburger (KM) equations (Koistinen & Marburger, 1959):

$$X_i^j = \hat{X}_A \check{X}_i (1 - \exp(-b(T) t_j^{n(T)})) \tag{9}$$

$$X_M = \hat{X}_A \check{X}_M (1 - \exp(-k_M (M_s - T))) \tag{10}$$

where X_i^j and X_M are the fractions of the phase (i) in the time (t_j) of the diffusional and the martensite transformation, respectively, $\hat{X}_A$ is the austenite fraction formed during heating stage, $\check{X}_i$ and $\check{X}_M$ are the maximum fractions of the phase (i) for diffusional and martensite transformation, respectively, calculated from the CCT diagram, $b(T)$ and $n(T)$ are diffusional transformation coefficients, k_M is the martensitic transformation coefficient and M_s is the martensitic transformation start temperature.

The phase transformations algorithm was also added to the model as a UDF. All UDFs used in the model were implemented in C++ and then compiled into a shared library. When running a simulation, Fluent loads: model file, data and material files, mesh file, and previously compiled UDF shared library files.

The proposed model concerns single-pass and single-beam welding. Each mesh node of the model heats up and then cools at a variable rate. To calculate the proportion of the phase formed during cooling in the HAZ, the average cooling rate in the range of 800–500°C is calculated using the formula:

$$v_{8/5} = \frac{800°\text{C} - 500°\text{C}}{t_{8/5}} \tag{11}$$

where $t_{8/5}$ is the cooling time in the range of 800−500°C.

4. Results and discussion

This section presents the calculation results of a laser welding model of a 12 mm thick plate made of S355J2 steel. The plate on which the welding tests were carried out was cut perpendicular to the welding direction in order to show the welding area. The cross-sectional specimens were made by grinding, polishing and then etching with 3% nital (3% solution of nitric acid and alcohol). These metallographic procedures revealed the structure and size of the FZ. Measurements of the depth (h) and radius (r) of the FZ were made, and the results are presented in Table 3. An additional parameter that characterizes the shape of the weld bead is the height to radius ratio of the FZ (h/r).

The heat source required the optimization of the following parameters: r_e, r_i and z_i, so that the calculated FZ had the size and shape as close as possible to that measured on the microstructure images (Tab. 3). The value $z_e = 0$ was assumed for all welding cases, i.e. the base of the conical heat source coincides with the upper plane of the welded sample (Fig. 4). The heat source parameters were optimized using a simple method of steepest descent. The least squares error function of h_c and r_c parameters was employed as an objective function. A series of simulations of the welding process made it possible to find the values of the cone dimensions, which are summarized in Table 4. In addition, Table 4 contains: depth (h_c), radius (r_c) and shape coefficient (h_c/r_c) of calculated FZ, average power density of conical heat source (P_v) and linear welding energy (E_l).

Table 3. Depth h and radius r of the FZ measured on microstructure images for two welding speeds v

v [m/min]	0.5					1.0				
P [W]	5000	4000	3000	2000	1000	5000	4000	3000	2000	1000
h [m]	0.00609	0.00587	0.00397	0.00147	0.00059	0.00529	0.00438	0.00307	0.00189	0.00042
r [m]	0.00166	0.00140	0.00171	0.00146	0.00083	0.00133	0.00105	0.00104	0.00118	0.00067
h/r	3.67	4.20	2.32	1.01	0.71	3.96	4.16	2.94	1.60	0.62

Table 4. The result of optimizing the dimensions of the conical heat source for the welding speed v = 0.5 and 1.0 m/min

v [m/min]	0.5					1.0				
P [W]	5000	4000	3000	2000	1000	5000	4000	3000	2000	1000
z_i [m]	0.00750	0.00670	0.00400	0.00148	0.00065	0.00620	0.00510	0.00330	0.00230	0.00105
r_e [m]	0.00140	0.00100	0.00115	0.00135	0.00175	0.00110	0.00095	0.00090	0.00110	0.00100
r_i [m]	0.00120	0.00090	0.00080	0.00070	0.00040	0.00100	0.00085	0.00080	0.00040	0.00050
h_c [m]	0.00619	0.00595	0.00382	0.00148	0.00063	0.00518	0.00446	0.00302	0.00173	0.00043
r_c [m]	0.00164	0.00134	0.00178	0.00141	0.00087	0.00129	0.00110	0.00098	0.00108	0.00069
h_c/r_c	3.78	4.43	2.14	1.05	0.73	4.03	4.05	3.09	1.61	0.62
P_v [W/m^3]	7.52E+10	1.26E+11	1.49E+11	1.78E+11	1.91E+11	1.47E+11	3.08E+11	4.00E+11	4.59E+11	5.20E+11
E_l [J/m]	360,000	288,000	216,000	108,000	61,200	189,000	144,000	90,000	60,000	30,000

The dimensions of the FZ measured on the microstructures (Tab. 3) and calculated using the presented welding model (Tab. 4) are summarized in Figures 5–7. For both welding speeds, the depth and width of the weld increase with the increase of the laser beam power (Fig. 5). The FZ ratio (h/r) increases with the laser power to 4 kW (Fig. 6). For a laser power of 5 kW, on the weld pool surface, the maximum calculated temperature increases significantly. In this case, the effect of the Marangoni force, which acts on the liquid surface towards the edge of the weld pool, increases. This widens the FZ at the top of the weld and decreases the aspect ratio (h/r).

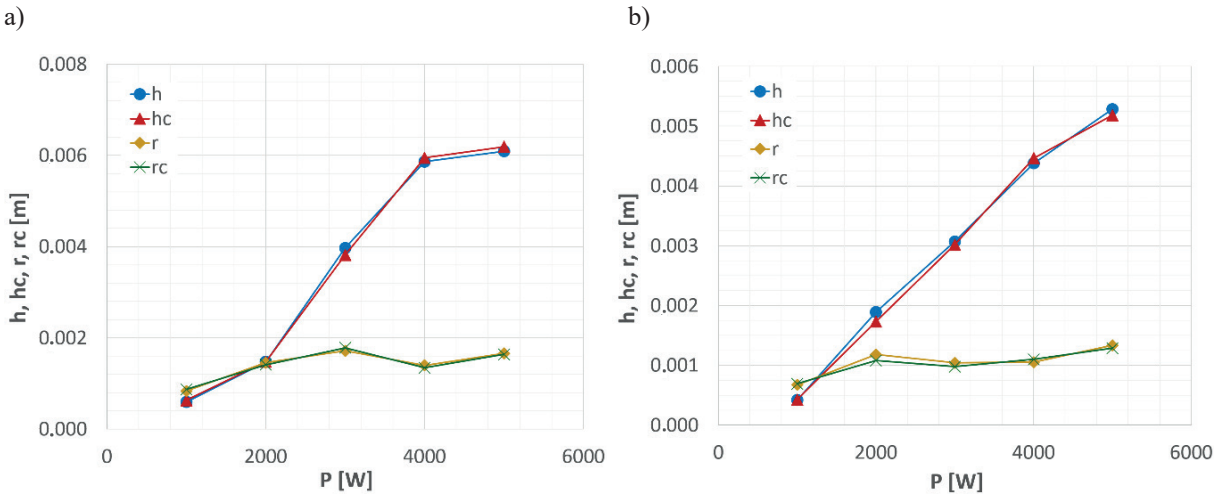

Fig. 5. Dependence of the depths (h, h_c) and radii (r, r_c) of the FZ on the laser power (P). The values were measured on microstructures and calculated in the welding model, respectively, for welding speeds of v = 0.5 m/min (a) and 1.0 m/min (b)

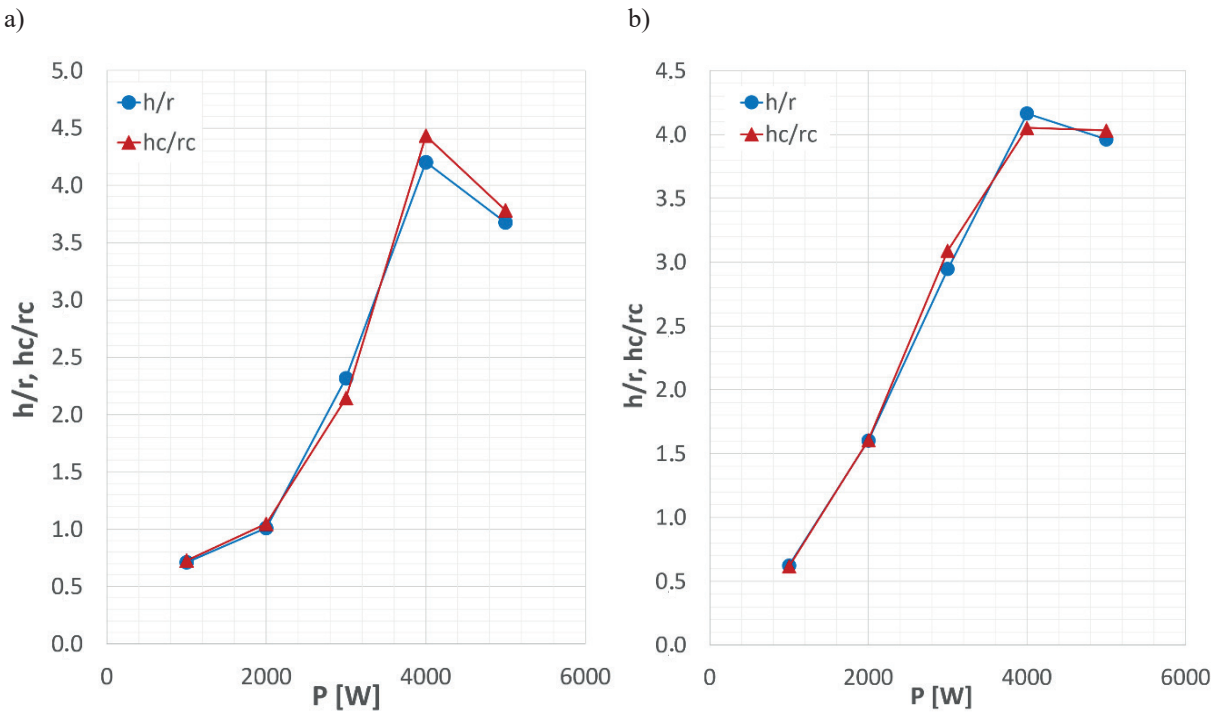

Fig. 6. Dependence of the weld shape coefficients (h/r, h_c/r_c) on the laser power (P). The values were measured on microstructures and calculated in the welding model, respectively, for welding speeds of v = 0.5 m/min (a) and 1.0 m/min (b)

For the optimized parameters of the conical heat source (Tab. 4), a graph of the relationship between the average power density (P_v) and the linear welding energy (E_l) was made (Fig. 7). As can be seen, for both welding speeds, there is a strong correlation between these two parameters up to 4 kW. As the linear welding energy increases, the average power density necessary to create a penetration of a given depth (h) and radius (r) decreases.

The ANSYS Fluent program was used to solve the numerical welding model. Material properties, initial and boundary conditions as well as heat source parameters were defined in the model. The solution of the system of energy and momentum equations made it possible to calculate the FZ and to track the phase changes occurring during cooling. The calculation results of the welding model were compared with the weld micrographs. Figures 8 and 9 contain sets of weld micrographs for the welding parameters used. The FZ, HAZ and the base material are visible as the distance from the welding line increases. The solidus temperature isotherm (T_{sol}) calculated for the optimized parameters of the heat source (Tab. 4) was plotted on the microstructure images. The points belonging to the isotherm reached the same maximum temperature throughout the welding process. Only the T_{sol} isotherm for S355J2 steel is shown in Figures 8 and 9, in order to compare the shape of the FZ on the micrograph. Temperature measurements in the model were carried out for a plane located at 2.5 mm away from the beginning of the weld bead. At this distance, the welding depth reaches its maximum value for the given welding conditions and does not change until the welding process simulation is completed. In the area near to the laser beam axis, the temperature exceeds the solidus temperature and a weld pool is formed there. The energy delivered to the welding area, at a lower welding speed of 0.5 m/min, is higher. This results in a deeper FZ compared to a welding speed of 1 m/min. The maximum temperature reached during the welding simulation, increases as the laser power increases. For laser power greater than 2 kW, the profile of FZ calculated with the model described in this article, is widened in the upper part of the weld. The Marangoni effect forces the liquid to flow towards the edges of the weld pool. This causes the edges to melt and widens the top of the weld pool.

Structural observations were carried out on metallographic specimens (Figs. 8, 9). The surface of the cross-sections is perpendicular to the weld and the fusion zone, heat-affected zone, and base material zone are visible. The martensitic structure is clearly visible in FZ, which was created during rapid cooling in the welding process. The Vickers microhardness tests were made on two sections at a distance of 1/3 and 2/3 of the fusion zone depth (h). The microhardness measurements were carried out using an Innovatest tester. Measurements were made at equal intervals of 0.15 mm, under load 25 gf. Measured hardness profiles for selected specimens are presented in Figure 10a, b. The hardness profile is symmetrical to the welding line. The higher hardness zone about 375 HV in the FZ decreases rapidly in the HAZ, to a hardness of about 180 HV in the base material zone. The hardness of the structure formed after welding is a function of the phases composition. Example distributions of martensite content calculated with the model for 4 kW laser welding are shown in Figure 10c, d.

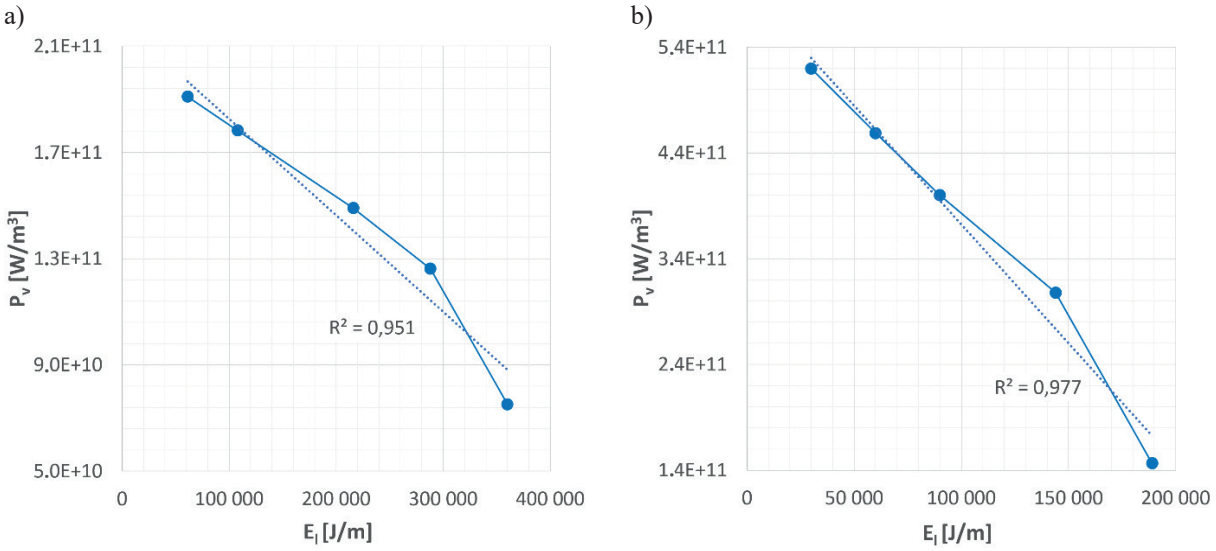

Fig. 7. Dependence of the average power density (P_v) on the linear welding energy (E_l), for the welding speed v = 0.5 m/min (a) and 1.0 m/min (b)

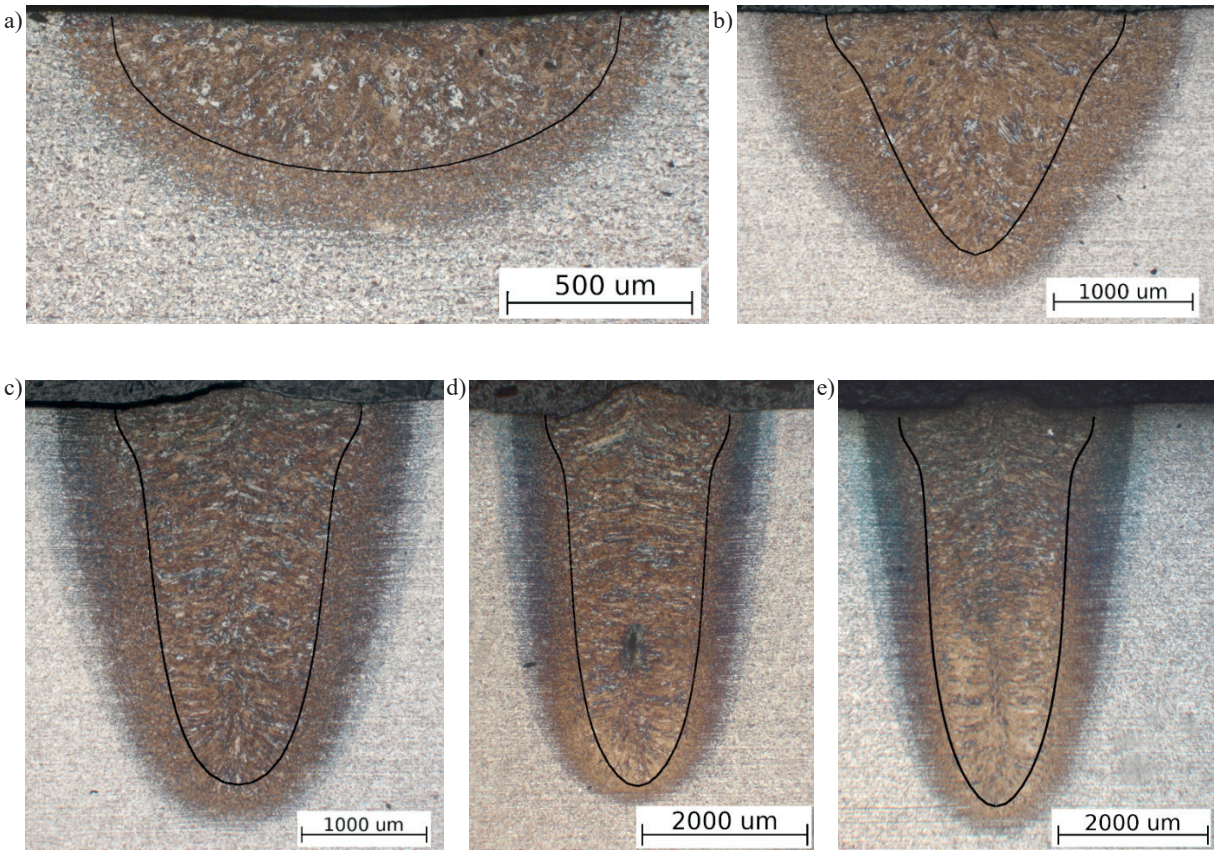

Fig. 8. Microstructure images of S355J2 steel welded with a 1 kW (a), 2 kW (b), 3 kW (c), 4 kW (d) and 5 kW (e) laser power at welding speed of 1.0 m/min. The isotherm line T_{sol} calculated with the model was plotted on the images

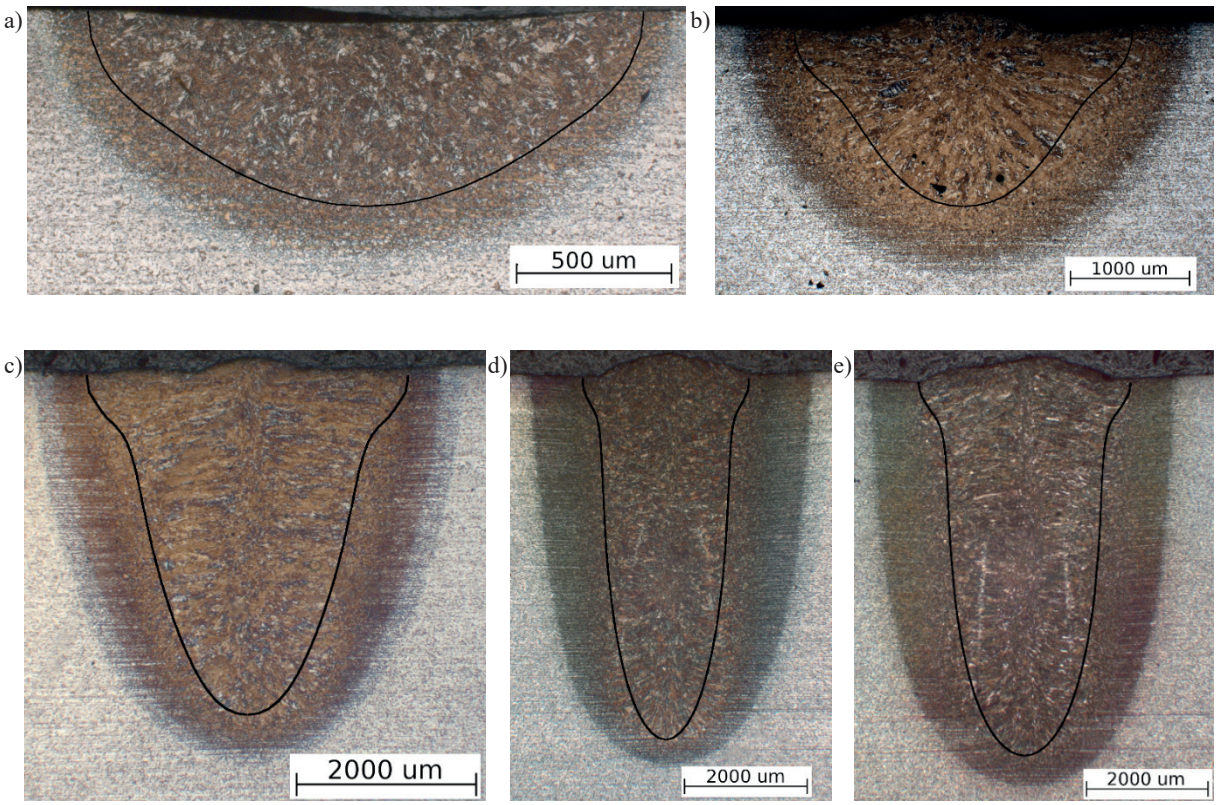

Fig. 9. Microstructure images of S355J2 steel welded with a 1 kW (a), 2 kW (b), 3 kW (c), 4 kW (d) and 5 kW (e) laser power at welding speed of 0.5 m/min. The isotherm line T_{sol} calculated with the model was plotted on the images

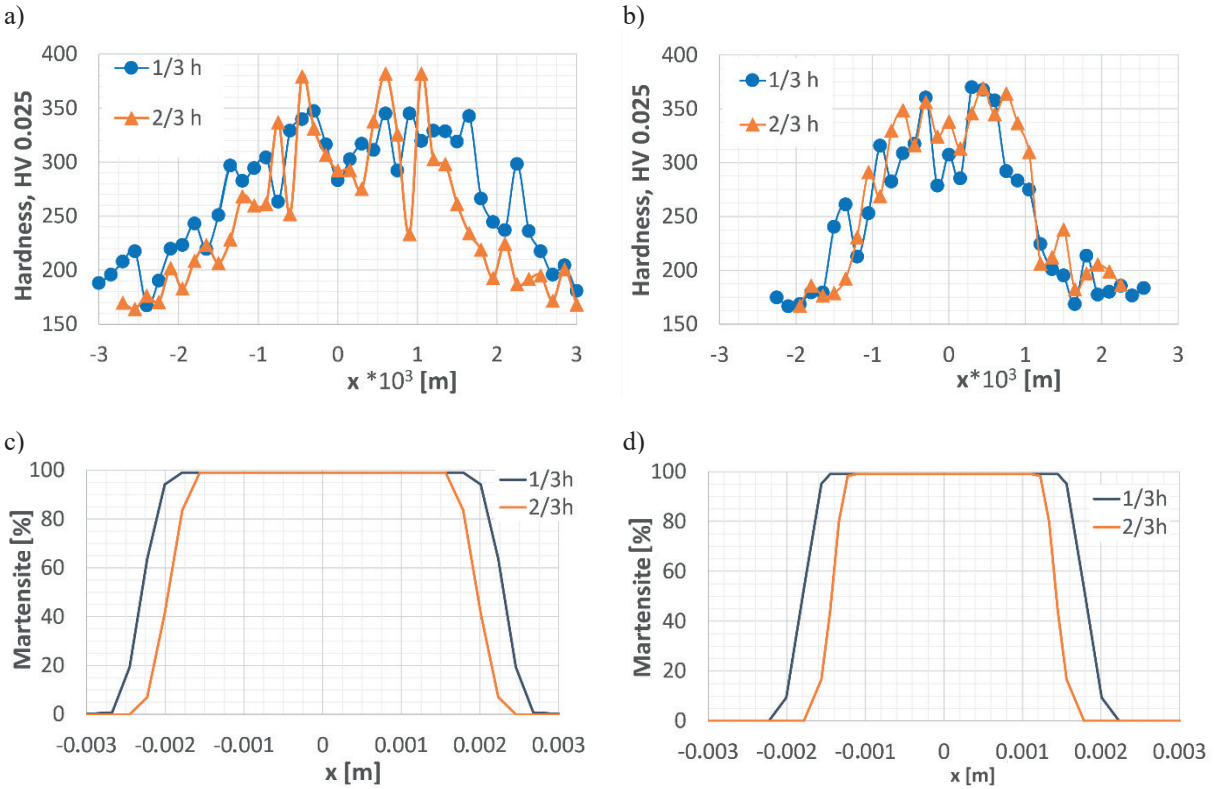

Fig. 10. Microhardness profile measured on the metallographic cross-section (a, b) and distribution of martensite content calculated with the model (c, d). Profiles for two cross-sections at a distance of 1/3 and 2/3 of the fusion zone depth (*h*) are presented. The data refer to samples welded with a 4 kW laser power at 0.5 m/min (a, c) and 1.0 m/min (b, d)

5. Summary and conclusions

This article describes a three-dimensional model of laser welding of S355J2 steel. The model implemented as additional UDF functions in the Fluent program calculates temperature fields, liquid metal flow rates, parameters of phase transformations and phase composition of steel after welding. The correctness of the model was verified experimentally in continuous welding tests with a Trumpf disc laser – TruDisk 12002 with a Trumpf D70 head, for various laser powers and welding speeds. Different shapes of the fusion lines were obtained by optimizing the dimensions of the conical heat source in the model. The comparison of microstructure images and model calculations revealed a high similarity of the geometry and dimensions of the FZ. The welding parameters adopted in the work result in high heating and cooling rates of the welded area. Phase transformations occurring during cooling are calculated using the CCT curves of S355J2 steel. The model-calculated phase composition of the welding area showed that the only transformation taking place at the selected parameters is the martensitic transformation. These results were confirmed by hardness measurements taken on metallographic cross-sections of the welded samples.

Based on the results, the following conclusions can be drawn:

- In order to obtain a more accurate shape of fusion, the surface tension function must be included in the welding model. The circulation of liquid forced by the surface tension expands the penetration zone in the upper part of the weld (e.g. Figs. 8e, 9e).
- Modeling the fusion zone shape using a volumetric heat source is accurate both in the conduction mode (e.g. Figs. 8a, 9a) and the keyhole mode (e.g. Figs. 8d, 9e). For the given welding conditions, convective heat transfer predominates (Pe~100). The size and shape of the weld are determined by convective flow in the weld pool.
- The presented model allows the tracking of the phase changes in the cooling stage. CCT data files are read by the UDF, therefore the model can be used for other steel grades. The calculated phase composition of the weld can be used to compare with the microhardness measurements (Fig. 10) and to estimate the hardness of the calculated structure.

– The volumetric heat source model requires the introduction of three parameters (z_i, r_e and r_i) to obtain the values (h_c and r_c) closest to the measured values (h, r). The shape factor (h/r) (Fig. 6) turned out to be an additional parameter that allowed to achieve a better fit of the fusion shape (Figs. 8 and 9). The measurement errors of the (h, r) was the same, while the error value of the shape factor (h/r) greater than one was more affected by the r error. The advantage of this approach is the achievement of optimal values of the heat source parameters in a smaller number of iterations.

– In the applied range of laser power and welding speed, a strong correlation was found between average power density (P_v) and linear welding energy (E_l) up to the laser power of 4 kW. The use of this correlation gives a better fit of the fusion line shape.

Acknowledgements

The research was supported by the Minister of Science and Higher Education, grant 16.16.110.663 and PL-Grid Infrastructure.

References

Ai, Y., Jiang, P., Shao, X., Wang, C., Li, P., Mi, G., Liu, Y., & Liu, W. (2016). An optimization method for defects reduction in fiber laser keyhole welding. *Applied Physics A*, *122*, 31. https://doi.org/10.1007/s00339-015-9555-8.

ANSYS 2021/R2 ANSYS (2021). *Fluent Theory Guide*. ANSYS Inc.

Avrami, M. (1939). Kinetics of phase change. I general theory. *Journal of Chemical Physics*, *7*(12), 1103–1112. https://doi.org/10.1063/1.1750380.

Bag, S., Trivedi, A., & De, A. (2009). Development of a finite element based heat transfer model for conduction mode laser spot welding process using an adaptive volumetric heat source. *International Journal of Thermal Sciences*, *48*(10), 1923–1931. https://doi.org/10.1016/j.ijthermalsci.2009.02.010.

BS-EN 1993-1-2:2005. *Eurocode 3: Design of steel structure general rules-structural fire design*. European Standard.

Chen, L., Mi, G., Zhang, X., & Wang, C. (2019). Numerical and experimental investigation on microstructure and residual stress of multi-pass hybrid laser-arc welded 316L steel. *Materials and Design*, *168*, 107653. https://doi.org/10.1016/j.matdes.2019.107653.

Dal, M., & Fabbro, R. (2016). An overview of the state of art in laser welding simulation. *Optics and Laser Technology*, *78*(A), 2–14. https://doi.org/10.1016/j.optlastec.2015.09.015.

Esfahani, M.N., Coupland, J., & Marimuthu, S. (2014). Microstructure and mechanical properties of a laser welded low carbon–stainless steel joint. *Journal of Materials Processing Technology*, 214 (12), 2941–294. https://doi.org/10.1016/j.jmatprotec.2014.07.001.

Farrokhi, F., Endelt, B., & Kristiansen, M. (2019). A numerical model for full and partial penetration hybrid laser welding of thick-section steels. *Optics and Laser Technology*, *111*, 671–686. https://doi.org/10.1016/j.optlastec.2018.08.059.

Goldak, J., Chakravarti, A., & Bibby, M. (1984). A new finite element model for welding, heat sources. *Metallurgical Transactions B*, *15B*, 299–305. https://doi.org/10.1007/BF02667333.

Ha, E.-J., & Kim, W.-S. (2005). A study of low-power density laser welding process with evolution of free surface. *International Journal of Heat and Fluid Flow*, *26*(4), 613–621. https://doi.org/10.1016/j.ijheatfluidflow.2005.03.009.

Han, L., & Liou, F.W. (2004). Numerical investigation of the influence of laser beam mode on melt pool. *International Journal of Heat and Mass Transfer*, *47*(19–20), 4385–4402. https://doi.org/10.1016/j.ijheatmasstransfer.2004.04.036.

Jie, X., & Hui, J. (2018). Numerical modeling of coupling thermal–metallurgical transformation phenomena of structural steel in the welding process. *Advances in Engineering Software*, *115*, 66–74. https://doi.org/10.1016/j.advengsoft.2017.08.011.

Ki, H., Mohanty, P.S., & Mazumder, J. (2002). Modeling of laser keyhole welding: Part I. Mathematical modeling, numerical methodology, role of recoil pressure, multiple reflections, and free surface evolution. *Metallurgical and Materials Transactions A*, *33A*, 1817–1830. https://doi.org/10.1007/s11661-002-0190-6.

Koistinen, D.P., & Marburger, R.E. (1959). A general equation describing extend of austenite-martensite transformation in pure Fe-C alloys and plain carbon steels. *Acta Metallurgica*, *7*(1), 59–60. https://doi.org/10.1016/0001-6160(59)90170-1.

Kumar, A., & DebRoy, T. (2004). Guaranteed fillet weld geometry from heat transfer model and multivariable optimization. *International Journal of Heat and Mass Transfer*, *47*(26), 5793–5806. https://doi.org/10.1016/j.ijheatmasstransfer.2004.06.038.

Laurens, P., Dubouchet, C., Kechemair, D., Coste, F., & Sabatier, L. (1996). Absorption dynamic behaviour of metals during CO_2 laser solid state treatments. *Journal of Physics D: Applied Physics*, *29*, 225–232. https://doi.org/10.1088/0022-3727/29/1/033.

Liu, S., Wu, Z., Liu, H., Zhou, H., Deng, K., Wang, C., Liu, L., Li, E. (2023). Optimization of welding parameters on welding distortion and stress in S690 high-strength steel thin-plate structures. *Journal of Materials Research and Technology*, *25*, 382–397. https://doi.org/10.1016/j.jmrt.2023.05.169.

Mollamahmutoglu, M., Yilmaz, O. (2021). Volumetric heat source model for laser-based powder bed fusion process in additive manufacturing. *Thermal Science and Engineering Progress*, *25*, 101021. https://doi.org/10.1016/j.tsep.2021.101021.

Mukherjee, T., De Manvatkar, V., A., & DebRoy, T. (2017). Dimensionless numbers in additive manufacturing. *Journal of Applied Physics*, *121*(6), 064904. https://doi.org/10.1063/1.4976006.

Pyo, C., Kim, J., Kim, Y., & Kim, M. (2022). A study on a representative heat source model for simulating laser welding for liquid hydrogen storage containers. *Marine Structures*, *86*, 103260. https://doi.org/10.1016/j.marstruc.2022.103260.

Rosenthal, D. (1941). Mathematical theory of heat distribution during welding and cutting. *Welding Journal*, *20*, 220–234.

Safdar, S., Pinkerton, A.J., Li, L., Sheikh, M.A., & Withers, P.J. (2013). An anisotropic enhanced thermal conductivity approach for modelling laser melt pools for Ni-base super alloys. *Applied Mathematical Modelling*, *37*(3), 1187–1195. https://doi.org/10.1016/j.apm.2012.03.028.

Sahoo, R., Debroy, T., & McNallan, M.J. (1988). Surface tension of binary metal – surface active solute systems under conditions relevant to welding metallurgy. *Metallurgical Transactions B*, *19B*, 483–491. https://doi.org/10.1007/BF02657748.

Semak, V., & Matsunawa, A. (1997). The role of recoil pressure in energy balance during laser materials processing. *Journal of Physics D: Applied Physics*, *30*(18), 2541–2552. https://doi.org/10.1088/0022-3727/30/18/008.

Semak, V.V., Steele, R.J., Fuerschbach, P.W., & Damkroger, B.K. (2000). Role of beam absorption in plasma during laser welding. *Journal of Physics D: Applied Physics*, *33*(10), 1179–1185. https://doi.org/10.1088/0022-3727/33/10/307.

Siwek, A. (2021). CFD-based modelling of phase transformation in laser welded low-carbon steel. *Welding in the World*, *65* (7), 1403–1414. https://doi.org/10.1007/s40194-021-01130-2.

Tsai, N.S., & Eagar, T.W. (1985). Distribution of the heat and current fluxes in gas tungsten arcs. *Metallurgical Transactions B*, *16B*, 841–846. https://doi.org/10.1007/BF02667521.

Wu, C.S., Wang, H.G., & Zhang, Y.M. (2006). A new heat source model for keyhole plasma arc welding in FEM analysis of the temperature profile. *Welding Journal*, *85* (12), 284–291.

Wu, C.S., Hu, Q.X., & Gao, J.Q. (2009). An adaptive heat source model for finite-element analysis of keyhole plasma arc welding. *Computational Materials Science*, *46*(1), 167–172. https://doi.org/10.1016/j.commatsci.2009.02.018.

Yan, S., Meng, Z., Chen, B., Tan, C., Song, X., & Wang, G. (2022). Prediction of temperature field and residual stress of oscillation laser welding of 316LN stainless steel. *Optics and Laser Technology*, *145*, 107493. https://doi.org/10.1016/j.optlastec.2021.107493.

Zhang, W., Kim, C.-H., & DebRoy, T. (2004). Heat and fluid flow in complex joints during gas metal arc welding – Part I: Numerical model of fillet welding. *Journal of Applied Physics*, *95*(9), 5210–5219. https://doi.org/10.1063/1.1699485.